nature photonics

Article

https://doi.org/10.1038/s41566-024-01434-x

Giant optical nonlinearity of Fermi polarons in atomically thin semiconductors

Received: 21 September 2023

Accepted: 25 March 2024

Published online: 14 May 2024

Check for updates

Liuxin Gu[1,9], Lifu Zhang[1,9], Ruihao Ni[1], Ming Xie[2], Dominik S. Wild[3], Suji Park[4], Houk Jang[4], Takashi Taniguchi[5], Kenji Watanabe[6], Mohammad Hafezi[7] & You Zhou[1,8]

Realizing strong nonlinear optical responses is a long-standing goal of both fundamental and technological importance. Recently, substantial efforts have been focused on exploring excitons in solids to achieve nonlinearities even down to few-photon levels. However, a crucial tradeoff arises as strong light–matter interactions require large oscillator strength and short radiative lifetime of excitons, which limits their nonlinearity. Here we experimentally demonstrate strong nonlinear optical responses with large oscillator strength by exploiting the coupling between excitons and carriers in an atomically thin semiconductor. By controlling the electric field and electrostatic doping of trilayer WSe_2, we observe the hybridization between intralayer and interlayer excitons and the formation of Fermi polarons. Substantial optical nonlinearity is observed under continuous-wave and pulsed laser excitation, where the Fermi polaron resonance blueshifts by as much as ~10 meV. Intriguingly, we observe a remarkable asymmetry in the optical nonlinearity between electron and hole doping, which is tunable by the applied electric field. We attribute these features to the optically induced valley polarization due to the interactions between excitons and free charges. Our results establish atomically thin heterostructures as a highly versatile platform for engineering nonlinear optical response with applications to classical and quantum optoelectronics.

Nonlinear optical phenomena lie at the heart of classical and quantum optics, with applications ranging from data communications to quantum control[1,2]. Developing physical systems with stronger optical nonlinearity and reducing their power requirement holds the promise for more efficient optoelectronics and may unlock new technologies such as single-photon switches and transistors[3–5]. In recent years, substantial efforts have been devoted to investigate excitons in semiconductors as a solid-state medium for realizing strong optical nonlinearity[6–8].

Also, van der Waals heterostructures based on atomically thin transition metal dichalcogenides (TMDs) have emerged as a new platform for the fundamental studies of excitons and for engineering optical responses[9,10]. Excitons in such two-dimensional materials are highly tunable with rich spin–valley physics and possess characteristics promising for optical nonlinearity, such as strong light–matter interactions and weak screening of Coulomb potential[10]. However, a major challenge in achieving high nonlinearity under low excitation

[1]Department of Materials Science and Engineering, University of Maryland, College Park, MD, USA. [2]Condensed Matter Theory Center, University of Maryland, College Park, MD, USA. [3]Max Plank Institute of Quantum Optics, Garching, Germany. [4]Center for Functional Nanomaterials, Brookhaven National Laboratory, Upton, NY, USA. [5]Research Center for Electronic and Optical Materials, National Institute for Materials Science, Tsukuba, Japan. [6]Research Center for Materials Nanoarchitectonics, National Institute for Materials Science, Tsukuba, Japan. [7]Joint Quantum Institute (JQI), University of Maryland, College Park, MD, USA. [8]Maryland Quantum Materials Center, College Park, MD, USA. [9]These authors contributed equally: Liuxin Gu, Lifu Zhang. e-mail: youzhou@umd.edu

https://doi.org/10.1038/s41566-024-01434-x

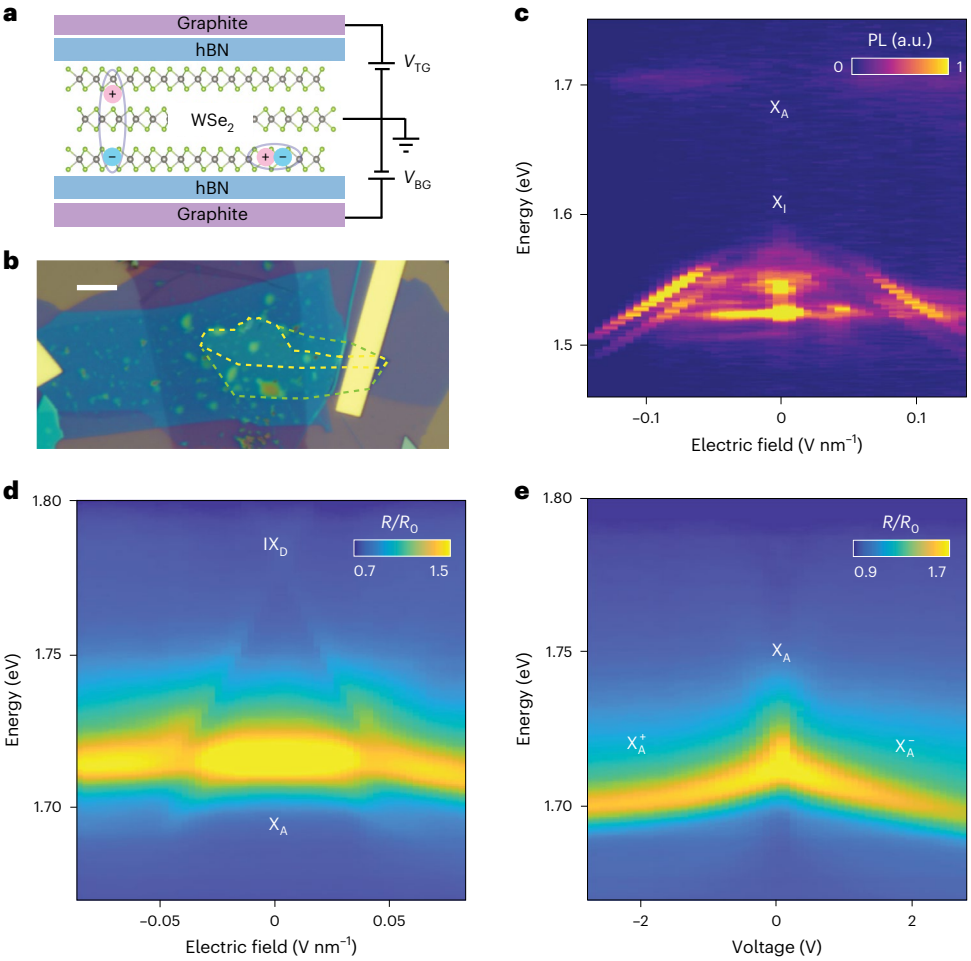

Fig. 1 | Dual-gated WSe_2 homotrilayer van der Waals heterostructure and their optical characteristics under gating at T = 4 K. a, Schematic of the trilayer vdW heterostructure. The homotrilayer WSe_2 is encapsulated with two hBN layers ~15–20 nm thick. **b**, Optical image of the homotrilayer WSe_2 device. Scale bar, 5 µm. The trilayer and neighbouring bilayer regions are enclosed by the yellow and green dashed lines, respectively. **c**, PL spectra of the WSe_2 trilayer under an electric field. The bright emission exhibiting a Stark shift under an electric field of 1.50–1.58 eV corresponds to the indirect exciton X_I. The upper weaker emission at 1.7 eV corresponds to the momentum-direct K–K intralayer exciton X_A. **d**, Reflectance spectra of the WSe_2 trilayer under an electric field. The high-energy momentum-direct K–K interlayer exciton shows a Stark shift of ~100 meV and begins to hybridize with X_A when their energies become degenerate around the electric field of 0.05 V nm^{-1}. **e**, Doping-dependent reflectance spectra of the WSe_2 trilayer. With increasing doping concentration, the intralayer trion or Fermi polaron (X_A^-/X_A^+) shifts towards lower energy.

power arises from the balance between the strengths of exciton–photon and exciton–exciton interactions[11–13]. For instance, intralayer excitons in these materials exhibit large oscillator strength but experience weak interactions, dominated by exchange interactions and limited by their short lifetime[14]. On the other hand, interlayer excitons in TMD heterostructures have longer lifetimes and experience interactions due to their finite electric dipole moment[15,16]. Unfortunately, the spatial separation of electron–hole wavefunctions leads to weaker absorption of incident photons. Several recent studies demonstrated enhanced interlayer exciton absorption via its hybridization with intralayer excitons in MoS_2 (refs. 6,17–19), although the oscillator strength of such hybrid excitons is still an order of magnitude weaker than the intralayer ones. So far, strong nonlinearity in intralayer excitons has not yet been realized. In this study, we report giant nonlinear optical responses of intralayer charged excitons, that is, Fermi polarons, on the order of several millielectronvolts under a photon flux of 10^{13} photons per second per square micrometre. This strong nonlinearity is highly tunable by the doping level and electric field, based on which we attribute the nonlinearity to an optically induced valley polarization resulting from exciton–carrier scattering.

Results

Electrical control of excitons

In our experiments, we encapsulate exfoliated WSe_2 homotrilayers inside two layers of hexagonal boron nitride (hBN) in a dual-gate geometry to independently control the overall doping levels and the displacement field (Fig. 1a,b). Figure 1c shows the photoluminescence (PL) map of the sample by varying the electric field and keeping the samples undoped. We observe strong emission from excitons X_I, whose energy linearly shifts with the electric field from 1.58 to 1.50 eV, and PL peaks at 1.71, 1.55 and 1.52 eV that remain constant with varying electric fields. We attribute the peak at 1.71 eV to intralayer momentum-direct exciton X_A at the K–K transition, based on their strong absorption (Fig. 1d) and zero Stark shift. The lower energy of X_I indicates that they are momentum-indirect excitons at the band edge, corresponding to transition across the indirect gap, located at the valence band Γ valleys and conduction band Q valleys, according to the band structure calculations[20–22]. From the linear Stark shift, we estimate the electric dipole of X_I to be around 0.78 nm e (Methods). The corresponding vertical displacement of the electron–hole pair in X_I is approximately half the distance between the top and bottom tungsten layers, indicating that the electrons or holes are partially layer delocalized.

https://doi.org/10.1038/s41566-024-01434-x

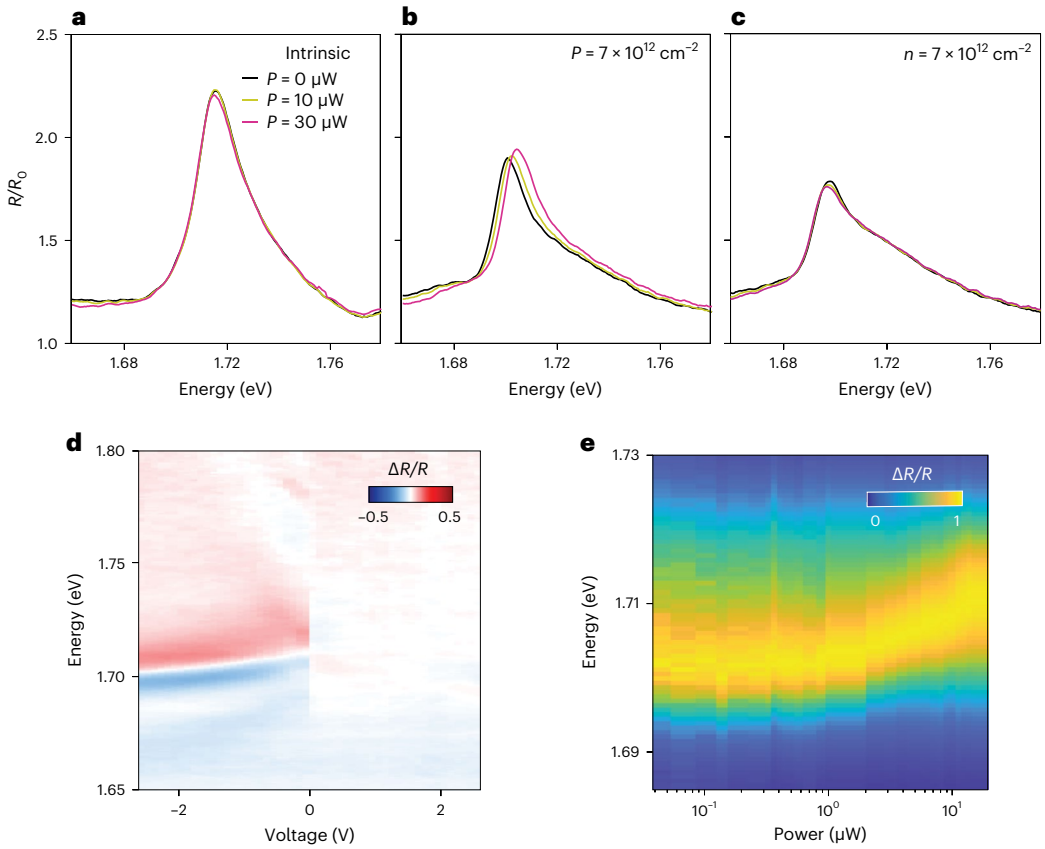

Fig. 2 | Nonlinearity in hole-doped homotrilayer WSe_2 at $T = 4$ K. **a**–**c**, Reflectance contrast R/R_0 of the trilayer under 0, 10 and 30 μW CW (635 nm) laser excitation with different doping levels, where R_0 is the reflectance of a reference region near the trilayer region with bare graphite/hBN/graphite on SiO_2 on the sample. Intriguingly, the exciton blueshifts when the sample is hole doped. **d**, Relative change in the reflectance induced by 30 μW of CW laser pumping under different doping levels. The colour map is obtained by normalizing the reflectance change induced by the CW excitation with respect to the reflectance without optical pumping, that is, $\Delta R/R = \frac{R_{(30\,\mu W)}}{R_{(\text{no pumping})}} - 1$. Therefore, a positive value (red colour) at high energy and negative value (blue) at low energy indicate a blueshift. The apparent discontinuity near 0 V is due to the high excitation power and finite voltage step used, and such a transition becomes smoother at lower excitation power (Supplementary Fig. 7 shows additional data). **e**, Blueshift of X_A^+ as a function of the pulsed laser excitation (718–720 nm, resonant with X_A^+) power, with a hole-doping level of 7×10^{12} cm^{-2}. The apparent redshift of the peak energy below 1 μW is due to fluctuations. In fact, X_A^+ consistently shifts towards higher energy with increasing power (Supplementary Fig. 8 shows additional data and analysis).

Next, we measure the reflectance of the trilayer under an electric field (Fig. 1d). In addition to the intralayer X_A, we observe an additional reflectance contrast at 1.78 eV (IX_D), which exhibits a substantial Stark effect of almost 100 meV (additional devices are shown in Supplementary Fig. 1). The finite reflection contrast and linear Stark effect of IX_D suggest that it corresponds to interlayer exciton at the direct K–K transition with larger oscillator strength than those momentum-indirect excitons, X_I, observed in PL. From the slope of the Stark effect, we estimate the electron–hole displacement to be 1.35 nm. Interestingly, as the energy of IX_D approaches that of the intralayer exciton X_A under a higher electric field, we observe an apparent anti-crossing behaviour of X_A and IX_D near the electric field of 0.05 V nm^{-1}. We note that the levels are not fully avoided and there is always finite reflection from X_A at 1.71 eV for all the electric fields, which will be comprehensively discussed later. To quantitatively understand the avoided crossing, we extract the exciton energies by fitting the reflectance spectra and then model the anti-crossing using a simple coupled oscillator model, from which we estimate a coupling strength of $W = 10 \pm 2$ meV between X_A and IX_D (Supplementary Fig. 2).

We further characterize how electrostatic gating modifies intralayer excitons X_A and their hybridization with interlayer excitons. Figure 1d shows the doping-dependent reflectance spectra of the sample under zero electric field. On doping, the reflectance from neutral X_A diminishes as they lose their oscillator strength, and the charged intralayer excitons emerge and shift to lower energies, with similar behaviours observed in PL (Supplementary Fig. 3). The redshift of the charged excitons with increasing doping levels can be explained in terms of an attractive Fermi polaron[23], or an increase in the exciton–trion energy splitting with increasing Fermi energy[24]. The similar doping dependence of reflectance and PL is due to the absence of Pauli blocking in both cases when the free carriers do not reside in the K valley[25]. As we focus on the highly doped regime where excitons interact with a large number of carriers, we refer to these charged excitons as Fermi polarons in later discussions[23].

Giant optical nonlinearity

Next, we study the excitons' nonlinear optical response by measuring the sample's reflectance spectra under different laser pumping levels. Figure 2a–c shows the reflectance spectra of the sample, probed with a halogen lamp as we excite the system with a 635 nm continuous-wave (CW) laser of different power values. When the trilayers are electron doped or intrinsic, optical pumping does not strongly alter the reflectance spectra. Intriguingly, however, in the hole-doped regime, optical pumping leads to a dramatic blueshift of the Fermi polaron X_A^+, on the order of a few millielectronvolts, and a slight linewidth increase under excitation of tens of microwatts (Fig. 2b). The oscillator strength of X_A^+, extracted from the reflection spectra, remains almost constant at low excitation power and decreases at higher power (Supplementary Fig. 4).

https://doi.org/10.1038/s41566-024-01434-x

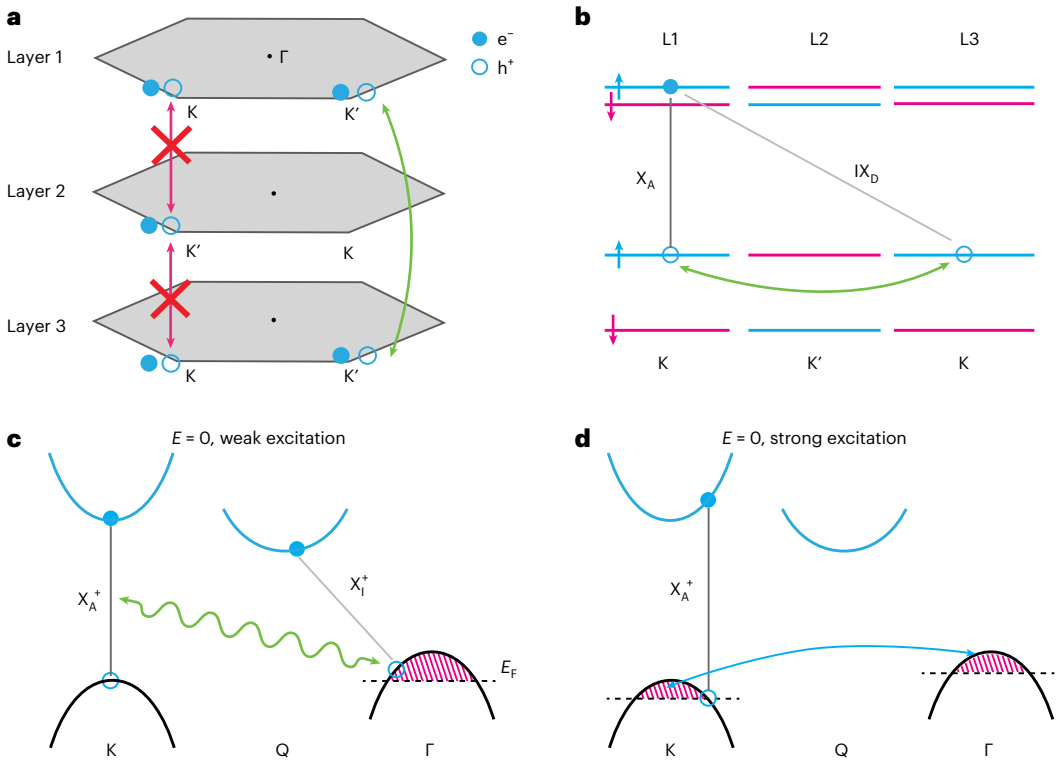

Fig. 3 | Electronic band structure of trilayer WSe_2. a, Crystal structure of natural trilayer WSe_2 dictates alternating K and K′ valleys among the neighbouring layers. The strong spin–orbit coupling of holes leads to weak tunnelling among the neighbouring layers but strong tunnelling between the top and bottom layers. **b**, Tunnelling of holes between the top and bottom layers results in the hybridization of intralayer K–K excitons X_A and interlayer K–K excitons IX_D. **c**,**d**, Band structures and carrier populations of hole-doped trilayer WSe_2 in the absence of an electric field ($E = 0$). **c**, Optical excitation generates both momentum-direct intralayer X_A^+ and momentum-indirect X_I of higher population. Intralayer Fermi polaron X_A^+ can interact with X_I and the free holes in the system. **d**, Under strong optical excitation, the interaction between intralayer excitons and free charges can induce a population transfer of carriers from the Γ to the K valley. The energy difference between Γ and K is small. The additional free carriers in the K valley lead to phase-space filling and optically induced blueshift of X_A^+. We note that in this non-equilibrium state, the dashed lines do not represent the Fermi level but are indications for the carrier population.

We note that PL signals are more than four orders of magnitude weaker than the reflected light and therefore negligible.

To visualize the doping dependence of nonlinearity, we measure the relative change in the sample's reflectance induced by optical pumping, $\Delta R/R = (R_p/R_{np}) - 1$, where R_p and R_{np} are the sample's reflectance spectra with and without laser pumping, respectively. Figure 2d shows the reflectance spectra $\Delta R/R$ under symmetric gating with zero electric field, where we observe striking asymmetry between the electron and hole sides. We briefly note that our observed nonlinearity of intralayer excitons is orders of magnitude stronger than that of dipolar interlayer excitons in bilayer TMDs[19,26] (Supplementary Table 1 lists a detailed comparison with other systems). Another critical distinction is that the nonlinearity in bilayer TMDs occurs for interlayer excitons in the intrinsic regime[6,19].

In addition to non-resonant excitation, we also probe the optical nonlinearity by resonantly exciting X_A with a pulsed laser (718–730 nm wavelength, ~100 ps pulse duration) and qualitatively observe similar nonlinear behaviours with an ~10 meV blueshift of X_A^+ and an increase in its linewidth, only on the hole-doped side (Fig. 2e and Supplementary Fig. 5). To investigate how excitation photon energies impact the nonlinearity, we tune the pulsed laser energy across the X_A^+ resonance. Resonant excitation results in a stronger blueshift than higher-energy excitation, whereas there is no noticeable shift of X_A^+ when the photon energy falls below X_A^+ (Supplementary Fig. 6). Additionally, we observe no strong wavelength dependence when the photon energy exceeds X_A^+ (Supplementary Fig. 6). In particular, the pulsed excitation generates an order of magnitude smaller blueshift than the CW laser at lower power with its peak power comparable with the CW laser's average power (Supplementary Fig. 8).

Optically induced valley polarization

The observed Stark effect and anti-crossing in WSe_2 trilayers can be understood by examining their crystal and band structure. In trilayers, each monolayer is rotated 180°, resulting in alternating K and K′ points between the layers[27] (Fig. 3a,b). Here we mainly consider the hole-tunnelling process, which is predicted to be much stronger than electron tunnelling by density functional theory calculations[28]. The sizeable spin–orbit coupling in the valence band dictates that the direct tunnelling between the neighbouring layers would be much weaker than that between the top and bottom layers across the middle layer (Fig. 3a,b). Such tunnelling leads to a finite oscillator strength of interlayer K–K excitons IX_D and their avoided crossing with intralayer X_A (ref. 29). Indeed, the experimentally extracted coupling strength between X_A and IX_D is consistent with the calculated interlayer coupling strength of holes at the K valley[22]. This is further corroborated by our measured dipole moment of IX_D being close to the distance between the top and bottom layers, and explains our observation that the level crossing at X_A is not fully avoided, since IX_D does not couple to intralayer excitons in the middle layer.

The observed optical nonlinearity and their doping dependence cannot be simply explained by heating or carrier injection from the laser since both effects result in a redshift of the intralayer excitons (Fig. 1e and Supplementary Fig. 9). Therefore, we examine how the interactions among the elementary excitations in the systems, that is, intralayer excitons X_A, momentum-indirect excitons X_I and free carriers, may give rise to the observed nonlinearity. First, we extract a large interaction strength of $g \approx 2$ meV μm² from the linear fit of energy blueshift versus X_A^+ density at low power[30] (Supplementary Fig. 8). It is apparent that excitonic interactions (that is, X_A–X_A and X_A–X_I) alone

https://doi.org/10.1038/s41566-024-01434-x

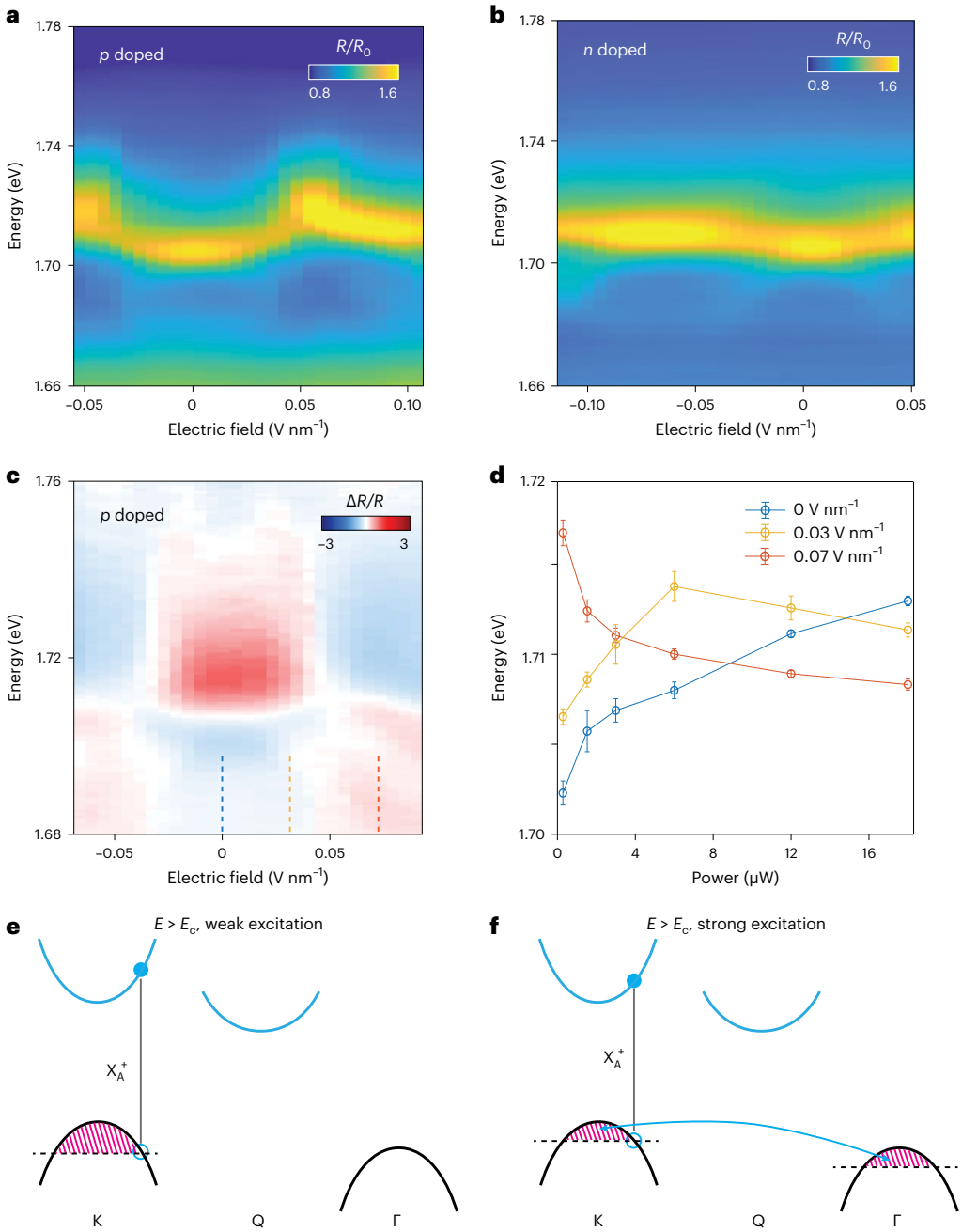

Fig. 4 | Electric-field-dependent exciton energy and nonlinearity in homotrilayer WSe_2 at $T = 4$ K. a,**b**, Electric-field dependence of the intralayer Fermi polaron reflectance contrast R/R_0 in a trilayer with a hole (**a**) and electron (**b**) doping density of 4.9×10^{12} cm^{-2}. **c**, Reflectance change induced by a pulsed laser excitation of 12 μW power. The colour map is obtained in the same way as that in Fig. 2d. Under a small electric field, X_A^+ shows a blueshift, but it begins to redshift under excitation at higher electric field. **d**, Line plots of the X_A^+-power-dependent peak shift under different electric fields. X_A^+ shows a blueshift of ~10 meV under zero applied electric field and a redshift of a similar magnitude under large electric field. The corresponding electric fields for these linecuts are indicated by the dashed lines in **c**. The error bars represent the uncertainty in determining the peak energy when fitting the reflection data. **e**,**f**, An electric field induces a shift of the valence band edge from the Γ to K valley. Under strong optical pumping, a net valley polarization is induced by exciton–carrier scattering with increased carriers at the Γ point, which leads to the optically induced redshift of X_A^+ at higher electric field. In the non-equilibrium states, the dashed lines are used as indications for the carrier populations, and do not represent the Fermi level.

cannot produce the observed nonlinearity. On one hand, X_A–X_A interactions among intralayer excitons are repulsive but weak, which scale linearly with density having coefficient $g_{ex} \approx \alpha E_B R^2 \approx 1.9$ μeV μm^2, where α is a constant (~6), $E_B \approx 100$ meV is the exciton binding energy and R (~1.78 nm) denotes the exciton Bohr radius in trilayers[31]. Given the short lifetime of X_A (almost picoseconds)[32,33] and thus the small density (~10^9 cm^{-2}; Methods), the amount of blueshift is expected to be orders of magnitude smaller than the experimental values (and comparable with monolayers and bilayers[20,31]). On the other hand, although X_A can acquire a dipole moment via its hybridization with IX_D and experience X_A–X_I dipolar interaction with X_I, such interactions should have persisted in the intrinsic and electron-doped regimes. Furthermore, we estimate an upper limit of dipolar interaction strength $g_d \approx 1.8$ μeV μm^2—orders of magnitude smaller than the experimental interaction strength g (Methods). This conclusion is supported by the experimental observation of the much weaker nonlinearity of X_I than X_A^+, even when

X_I is fully polarized by an external electric field (Methods and Supplementary Fig. 10 provide additional discussion).

Therefore, we attribute the observed nonlinearity to the valley polarization created from the interactions between X_A and free carriers. In particular, excitons created by optical pumping may induce a non-equilibrium valley population imbalance in the resident carriers between the K and Γ valleys, via mechanisms such as exciton–carrier scattering[34,35]. Importantly, under zero electric field, the energy difference between the K and Γ valleys is rather small in trilayers[22], on the order of tens of millielectronvolts, based on first-principle calculations and transport studies (Fig. 3c). As a result, electrostatically doped holes at the Γ point could be efficiently scattered into the K valley by excitons such as X_A and X_I, via Coulombic and exchange interactions[34,35] (Fig. 3d). This net accumulation of the valley population at K (and K′) induces phase-space filling and consequently the observed blueshift of X_A^+. Such a scattering process would also introduce additional dephasing, which explains the increase in X_A^+ linewidth. Meanwhile, the oscillator strength remains unchanged at low excitation power, since it depends on the total doping level, but decreases at higher power due to saturation. In addition to the exciton–carrier scattering, the net valley polarization may also be created by the electric field induced by optical pumping. For instance, in bilayer TMDs, it has been suggested that the generation of dipolar X_I excitons may create a non-zero displacement field due to spontaneous symmetry breaking[6]. Such a displacement field can introduce a relative energy shift between the K and Γ valleys[22], thereby creating a valley polarization. To further investigate such possible valley polarization, we probe the population of the resident carriers in the K and K′ valleys under circularly polarized resonant excitation. As shown in Supplementary Fig. 11, we observe a stronger blueshift of X_A^+ in the K than K′ valley when exciting excitons in the K valley, consistent with our optically induced valley polarization picture.

The proposed valley polarization mechanism also explains the strong electron–hole asymmetry of optical nonlinearity. Intrinsic trilayer WSe_2 exhibits weak nonlinearity, since no valley polarization can be created without resident carriers. In the electron-doped case, the valley polarization of resident carriers is prevented by the much larger energy splitting, on the order of hundreds of millielectronvolts, between the Q (band minimum) and K (where X_A reside) valleys in the conduction band[22]. We also briefly note that in TMD monolayers, optical pumping with circularly polarized light can polarize carriers in K versus K′ valleys[32–38]. The generation of valley imbalance in monolayers has been attributed to mechanisms such as different intervalley versus intravalley carrier relaxation rates, as well as different indirect excitons and spin-forbidden dark exciton relaxation rates[39,40]. Unlike in the monolayer case, where a spin flip of carriers is required for scattering between the K and K′ valleys, the Γ point is spin-degenerate such that the intervalley scattering between K and Γ in trilayers can happen via a spin-conserving process, such as direct Coulomb and exchange interactions between holes and excitons. We note that X_I probably plays a crucial role in exciton–electron scattering owing to its larger population than X_A (Supplementary Fig. 10 shows the estimated X_I density). Since the relaxation processes of X_A to X_I and X_I to the ground state both involve finite momentum transfer, they can facilitate the valley polarization process via exciton–carrier scattering. This suggests that the dynamics of valley polarization could occur at a timescale similar to the X_I lifetime, on the order of nanoseconds, which may explain our observation of weaker nonlinearity created by the pulsed laser than CW with the same peak power (Supplementary Fig. 8).

To further corroborate our hypothesis, we control the relative energies of the Γ and K valleys by applying an external electric field[20,22], and study the resulting changes in both energies and optical nonlinearity of Fermi polarons. First, we measure the reflectance of X_A^+ and X_A^- as we change the electric field under fixed doping levels (Fig. 4a,b). With an increasing field, the energy of the X_A^+ blueshifts at a smaller electric field and then switches to redshift above an electric field of ~0.05 V nm^{-1} (Fig. 4a). The electric field shifts the valence band maximum from Γ to K due to the distinct orbit characters of the eigenstates[22]. Although the eigenstate at K becomes layer polarized at higher energies with the field, the wavefunction at the Γ point features a large interlayer coupling with small energy change under the field[22]. This shift from Γ to K leads to more phase-space filling in K and a blueshift in X_A^+, consistent with our proposed mechanism for optical nonlinearity (Supplementary Fig. 13). Above an electric field of ~0.05 V nm^{-1}, X_A^+ begins to redshift. This electric field is comparable with the critical field under which the band edge shifts from Γ to K, as determined from the transport studies[22] (note that the field reported in the literature differs from our definition by a factor of the relative dielectric constant). In stark contrast, the energy shift of X_A^- is much smaller in the electron-doped region (Fig. 4b), where the band edge remains at the Q point. The small energy variation of X_A^- can be explained by the avoided crossing similar to the undoped case (Supplementary Fig. 1).

Intriguingly, the electric field also dramatically changes the nonlinear responses of X_A^+. As shown in Fig. 4c, the reflectance change induced by optical pumping, that is, $\Delta R/R$, shows a clear flip in the colour contract at ~0.05 V nm^{-1}, which coincides with the crossover field between the blueshift and redshift of X_A^+ (Fig. 4a). The magnitude of blueshift and redshift is similar under the same excitation condition, around 10 meV (Fig. 4d). Such electric-field control of optical nonlinearity provides additional supporting evidence for our proposed mechanism involving valley polarization (Fig. 4e,f). Figure 4e shows the modified band structure above the critical field[22]. Under optical excitation, the same exciton–hole scattering process can induce a population transfer of holes from K to Γ, as well as reduce the X_A^+ energies (Fig. 4f). This also explains the similar critical electric fields where both nonlinearity and electric-field susceptibility turn from blue- to redshift.

Conclusion

Our results demonstrating highly nonlinear excitons with large oscillator strengths open avenues for engineering exciton–carrier interactions in atomically thin heterostructures to explore strongly interacting many-body physics and develop novel optoelectronics. By designing the atomic and electronic structures of the heterostructures, one may engineer the strong interactions between bright and dark excitons and free charges[26]. The excitonic and free-charge populations are highly tunable, and elucidating the complex interactions between intralayer and interlayer excitons and charges will be of great future interest for studying many-body physics in a hybrid Fermi–Bose system[41–43], from both theoretical and experiment perspectives. These strongly interacting optical excitations can be used to realize active nonlinear metasurfaces based on the spatial confinement of excitons by moiré superlattice and local electrostatic gate[44–46]. Combining strong nonlinearity with spatial confinement could also further boost nonlinearity and allow exploring quantum optical effects, including non-classical light sources and few-photon nonlinearity[11,47]. Although current experiments require 10^3–10^4 photons to shift the resonance by a linewidth, improving materials quality and engineering photonic environment could substantially lower the required photon count by reducing the Fermi polaron linewidth. Finally, the demonstrated optical control of exciton resonances could enable novel nonlinear optoelectronic devices such as all-optical switching, nonlinear optomechanical resonators[48,49] and optical limiting devices[1,50].

Online content

Any methods, additional references, Nature Portfolio reporting summaries, source data, extended data, supplementary information, acknowledgements, peer review information; details of author contributions and competing interests; and statements of data and code availability are available at https://doi.org/10.1038/s41566-024-01434-x.

References

1. Volz, T. et al. Ultrafast all-optical switching by single photons. *Nat. Photon.* **6**, 605–609 (2012).

2. Boyd, R. W. *Nonlinear Optics* (Academic Press, 2003).
3. Zasedatelev, A. V. et al. Single-photon nonlinearity at room temperature. *Nature* **597**, 493–497 (2021).
4. Chang, D. E., Sørensen, A. S., Demler, E. A. & Lukin, M. D. A single-photon transistor using nanoscale surface plasmons. *Nat. Phys.* **3**, 807–812 (2007).
5. Sun, S., Kim, H., Luo, Z., Solomon, G. S. & Waks, E. A single-photon switch and transistor enabled by a solid-state quantum memory. *Science* **361**, 57–60 (2018).
6. Datta, B. et al. Highly nonlinear dipolar exciton–polaritons in bilayer MoS_2. *Nat. Commun.* **13**, 6341 (2022).
7. Delteil, A. et al. Towards polariton blockade of confined exciton–polaritons. *Nat. Mater.* **18**, 219–222 (2019).
8. Muñoz-Matutano, G. et al. Emergence of quantum correlations from interacting fibre-cavity polaritons. *Nat. Mater.* **18**, 213–218 (2019).
9. Mak, K. F. & Shan, J. Opportunities and challenges of interlayer exciton control and manipulation. *Nat. Nanotechnol.* **13**, 974–976 (2018).
10. Wilson, N. P., Yao, W., Shan, J. & Xu, X. Excitons and emergent quantum phenomena in stacked 2D semiconductors. *Nature* **599**, 383–392 (2021).
11. Wild, D. S., Shahmoon, E., Yelin, S. F. & Lukin, M. D. Quantum nonlinear optics in atomically thin materials. *Phys. Rev. Lett.* **121**, 123606 (2018).
12. Liu, X. et al. Strong light–matter coupling in two-dimensional atomic crystals. *Nat. Photon.* **9**, 30–34 (2015).
13. Barachati, F. et al. Interacting polariton fluids in a monolayer of tungsten disulfide. *Nat. Nanotechnol.* **13**, 906–909 (2018).
14. Regan, E. C. et al. Emerging exciton physics in transition metal dichalcogenide heterobilayers. *Nat. Rev. Mater.* **7**, 778–795 (2022).
15. Zhang, L. et al. Highly valley-polarized singlet and triplet interlayer excitons in van der Waals heterostructure. *Phys. Rev. B* **100**, 041402 (2019).
16. Rivera, P. et al. Valley-polarized exciton dynamics in a 2D semiconductor heterostructure. *Science* **351**, 688–691 (2016).
17. Walther, V., Johne, R. & Pohl, T. Giant optical nonlinearities from Rydberg excitons in semiconductor microcavities. *Nat. Commun.* **9**, 1309 (2018).
18. Leisgang, N. et al. Giant Stark splitting of an exciton in bilayer MoS_2. *Nat. Nanotechnol.* **15**, 901–907 (2020).
19. Louca, C. et al. Interspecies exciton interactions lead to enhanced nonlinearity of dipolar excitons and polaritons in MoS_2 homobilayers. *Nat. Commun.* **14**, 3818 (2023).
20. Wang, Z., Chiu, Y. H., Honz, K., Mak, K. F. & Shan, J. Electrical tuning of interlayer exciton gases in WSe_2 bilayers. *Nano Lett.* **18**, 137–143 (2018).
21. Scuri, G. et al. Electrically tunable valley dynamics in twisted WSe_2/WSe_2 bilayers. *Phys. Rev. Lett.* **124**, 217403 (2020).
22. Movva, H. C. P. et al. Tunable Γ-K valley populations in hole-doped trilayer WSe_2. *Phys. Rev. Lett.* **120**, 107703 (2018).
23. Sidler, M. et al. Fermi polaron–polaritons in charge-tunable atomically thin semiconductors. *Nat. Phys.* **13**, 255–261 (2017).
24. Mak, K. F. et al. Tightly bound trions in monolayer MoS_2. *Nat. Mater.* **12**, 207–211 (2013).
25. Wang, Z., Zhao, L., Mak, K. F. & Shan, J. Probing the spin-polarized electronic band structure in monolayer transition metal dichalcogenides by optical spectroscopy. *Nano Lett.* **17**, 740–746 (2017).
26. Erkensten, D., Brem, S. & Malic, E. Exciton–exciton interaction in transition metal dichalcogenide monolayers and van der Waals heterostructures. *Phys. Rev. B* **103**, 045426 (2021).
27. Jones, A. M. et al. Spin-layer locking effects in optical orientation of exciton spin in bilayer WSe_2. *Nat. Phys.* **10**, 130–134 (2014).
28. Gong, Z. et al. Magnetoelectric effects and valley-controlled spin quantum gates in transition metal dichalcogenide bilayers. *Nat. Commun.* **4**, 2053 (2013).
29. Zhang, Y. et al. Every-other-layer dipolar excitons in a spin–valley locked superlattice. *Nat. Nanotechnol.* **18**, 501–506 (2023).
30. Stepanov, P. et al. Exciton–exciton interaction beyond the hydrogenic picture in a $MoSe_2$ monolayer in the strong light–matter coupling regime. *Phys. Rev. Lett.* **126**, 167401 (2021).
31. Scuri, G. et al. Large excitonic reflectivity of monolayer $MoSe_2$ encapsulated in hexagonal boron nitride. *Phys. Rev. Lett.* **120**, 37402 (2018).
32. Wang, G. et al. Valley dynamics probed through charged and neutral exciton emission in monolayer WSe_2. *Phys. Rev. B* **90**, 075413 (2014).
33. Hsu, W.-T. et al. Optically initialized robust valley-polarized holes in monolayer WSe_2. *Nat. Commun.* **6**, 8963 (2015).
34. Courtade, E. et al. Charged excitons in monolayer WSe_2: experiment and theory. *Phys. Rev. B* **96**, 085302 (2017).
35. Fey, C., Schmelcher, P., Imamoglu, A. & Schmidt, R. Theory of exciton–electron scattering in atomically thin semiconductors. *Phys. Rev. B* **101**, 195417 (2020).
36. Yan, T., Yang, S., Li, D. & Cui, X. Long valley relaxation time of free carriers in monolayer WSe_2. *Phys. Rev. B* **95**, 241406 (2017).
37. Goryca, M., Wilson, N. P., Dey, P., Xu, X. & Crooker, S. A. Detection of thermodynamic 'valley noise' in monolayer semiconductors: access to intrinsic valley relaxation time scales. *Sci. Adv.* **5**, eaau4899 (2019).
38. Yang, L. et al. Long-lived nanosecond spin relaxation and spin coherence of electrons in monolayer MoS_2 and WS_2. *Nat. Phys.* **11**, 830–834 (2015).
39. Dery, H. & Song, Y. Polarization analysis of excitons in monolayer and bilayer transition-metal dichalcogenides. *Phys. Rev. B* **92**, 125431 (2015).
40. Robert, C. et al. Spin/valley pumping of resident electrons in WSe_2 and WS_2 monolayers. *Nat. Commun.* **12**, 5455 (2021).
41. Park, H. et al. Dipole ladders with large Hubbard interaction in a moiré exciton lattice. *Nat. Phys.* **19**, 1286–1292 (2023).
42. Gao, B. et al. Excitonic Mott insulator in a Bose–Fermi–Hubbard system of moiré WS_2/WSe_2 heterobilayer. *Nat. Commun.* **15**, 2305 (2024).
43. Xiong, R. et al. Correlated insulator of excitons in WSe_2/WS_2 moiré superlattices. *Science* **380**, 860–864 (2023).
44. Koshelev, K. et al. Subwavelength dielectric resonators for nonlinear nanophotonics. *Science* **367**, 288–292 (2020).
45. Bekenstein, R. et al. Quantum metasurfaces with atom arrays. *Nat. Phys.* **16**, 676–681 (2020).
46. Cai, T. et al. Radiative enhancement of single quantum emitters in WSe_2 monolayers using site-controlled metallic nanopillars. *ACS Photonics* **5**, 3466–3471 (2018).
47. Yu, H., Liu, G. B., Tang, J., Xu, X. & Yao, W. Moiré excitons: from programmable quantum emitter arrays to spin–orbit-coupled artificial lattices. *Sci. Adv.* **3**, e1701696 (2017).
48. Zhou, Y. et al. Controlling excitons in an atomically thin membrane with a mirror. *Phys. Rev. Lett.* **124**, 27401 (2020).
49. Aspelmeyer, M., Kippenberg, T. J. & Marquardt, F. Cavity optomechanics. *Rev. Mod. Phys.* **86**, 1391–1452 (2014).
50. Van Stryland, E. W., Wu, Y. Y., Hagan, D. J., Soileau, M. J. & Mansour, K. Optical limiting with semiconductors. *J. Opt. Soc. Am. B* **5**, 1980–1988 (1988).

Methods

Device fabrication

Graphite and hBN flakes are mechanically exfoliated from the bulk crystals onto the silicon chip with a SiO_2 layer. Some of the exfoliated homotrilayer WSe_2 flakes were provided by the Quantum Material Press facility in the Center for Functional Nanomaterials at Brookhaven National Laboratory. The thickness of the hBN flakes and WSe_2 layer numbers are estimated on the basis of the colour contrast under optical microscopy. The heterostructure is assembled in a transfer station built by Everbeing Int'l Corp., which uses polydimethylsiloxane and polycarbonate as the stamp and all the flakes are transferred in a dry transfer method onto a silicon chip with a 285 nm SiO_2 layer. Then, the electrical contacts are patterned by electron-beam lithography and a liftoff process where we deposited 5 nm Cr and 80 nm Au by thermal evaporation.

Optical spectroscopy

The optical measurements were performed in our home-built confocal microscope with an attoDRY 4K cryostat. The apochromatic objective equipped in the chamber has a numerical aperture of 0.82. The PL measurement is performed under 635 nm diode laser excitation. The reflectance measurement is performed using either a halogen lamp (Thorlabs) or a supercontinuum white laser (YSL Photonics) as the excitation source. The diode laser has a diffraction-limited spot size, whereas the beam diameter of the white laser is slightly larger—around 1 µm. The white laser has a pulse duration of ~60 ps with a variable repetition rate of up to 40 MHz. Our power-dependent reflectance is measured under both CW and pulsed excitation. In CW measurements, we illuminate the sample with a halogen lamp as the probe and use the CW (635 nm) diode laser as excitation, with power ranging from 0.02 to 30.00 µW. In the pulsed resonant excitation case, we excite the system with a supercontinuum white laser filtered in the 718–730 nm wavelength range. We vary the incident power and directly measure the reflected white laser signal from the sample. In both cases, our reflectance spectra are normalized by dividing the reflected light intensity from the sample trilayer area by the reflected light intensity from the nearby bare hBN on the SiO_2 area. The spectra are measured by a Horiba iHR320 spectrometer using a 300 mm $line^{-1}$ grating and a Synapse+ BIDD charge-coupled device camera.

Doping density and electric field

The doping density and electric field are determined by considering the heterostructure as a parallel capacitor[30]. The applied electric field is calculated as $E = \frac{D}{\varepsilon_0 \varepsilon_{WSe2}}$, whereas the displacement field D is determined as $D = \frac{1}{2}(C_{Top} \times \Delta V_{TG} - C_{Bottom} \times \Delta V_{BG})$. The top and bottom capacitances are given by $C_{Top(Bottom)} = \frac{\varepsilon_0 \varepsilon_{hBN}}{t_{hBN}}$, where t is the thickness of the top and bottom hBN layer. ΔV_T and ΔV_B are the applied top-gate and bottom-gate voltages relative to the offset voltage to the band edge, respectively. The total doping density in the system can be determined as $n = \frac{1}{e} \times (C_{Top} \times \Delta V_{TG} + C_{Bottom} \times \Delta V_{BG})$. We use $\varepsilon_{WSe2} = 7$ (refs. 33,41) and $\varepsilon_{hBN} = 3$ (ref. 41) in our case. The thicknesses of the hBN layers are extracted by atomic force microscopy measurements.

Extract dipole distance *d*

The energy shift as a function of the electric field of IX_D and X_I obeys the law of Stark shift, which can be described as follows:

$$\Delta E = |e \times d \times E| = |e \times d \times \frac{\varepsilon_{hBN}}{\varepsilon_{WSe2}} \times \frac{V_{BG}}{t_{BG}}|. \quad (1)$$

Thus, the dipole moment of excitons can be calculated as

$$d = |\frac{\Delta E}{e} \times \frac{\varepsilon_{WSe2}}{\varepsilon_{hBN}} \times \frac{t_{BG}}{V_{BG}}|. \quad (2)$$

Estimate of exciton density

In the steady state, the exciton densities of both intra- and interlayer excitons can be estimated by $n_X = I\alpha\tau/A\hbar\omega$, where I is the pump power, A is the pump-beam size, $\hbar\omega$ is the photon energy, α is the sample's absorbance at the pump wavelength and τ is the lifetime of respective excitons. The lifetime of interlayer excitons X_I is estimated from time-dependent PL measurements, whereas we take the lifetime of X_A from the literature.

The density of X_I can be estimated from an independent method by measuring their PL and considering dipolar interactions using a simple capacitor model in which the exciton density is proportional to the blueshift induced by the repulsion between excitons[20]: $n_X = \frac{\varepsilon_0 \varepsilon_{TMD} \times \Delta E}{de^2}$, where ΔE is the blueshift of the emission energy and d is the dipole moment of X_I, estimated to be ~0.78 nm from the Stark effect.

Estimate of exchange and dipolar interaction strengths

The exchange interaction strength can be estimated from $g_{ex} \approx \alpha E_B R^2$, where α is a constant, E_B is the exciton binding energy and R denotes the exciton Bohr radius in trilayers. For our calculation, we adopt $\alpha = 6$, E_B of ~100 meV and R of 1.78 nm, which are values from the literature[31], to estimate the interaction strength.

Meanwhile, X_A could acquire finite electrical dipoles via its hybridization with IX_D. We note that to the first order, there should be zero net dipoles and weak dipolar interactions under symmetric gating. However, the emergence of local net dipoles is plausible due to spontaneous symmetry breaking. In light of this, we calculate an upper limit for the dipolar interactions, assuming all the dipoles are aligned. Using a parallel-plate model, the dipolar interaction strength is given by $g_d = \frac{e^2 d}{\varepsilon_0 \varepsilon_{TMD}}$, where ed is the dipole moment of X_A. This dipole moment, ed, acquired from the hybridization with IX_D, can be estimated from the composition percentage of each exciton species in the coupled oscillator model (Supplementary Fig. 2). The value peaks when X_A becomes degenerate with IX_D, reaching ~0.7 nm e, thereby leading to an estimated dipolar interaction strength of $g_d \approx 1.7$ µeV µm^2.

Estimate of photon numbers required to shift the resonance by a linewidth

The photon numbers are calculated from $n = \frac{P\tau}{E}$, where P is the power of the laser, τ is the Fermi polaron lifetime and $E = \frac{hc}{\lambda}$ is the photon energy. For pulsed laser excitation, we convert the average pumping power (P_{Avg}) into peak power $P = \frac{P_{Avg}}{f_R \times t_p}$, where f_R is the repetition rate and t_p is the pulse duration.

Data availability

All other data are available from the corresponding author upon reasonable request. Source data are provided with this paper.

Acknowledgements

This research is primarily supported by the US Department of Energy, Office of Science, Office of Basic Energy Sciences Early Career Research Program, under award no. DE-SC-0022885. The fabrication of samples is supported by the National Science Foundation CAREER Award under award no. DMR-2145712. This research used Quantum Material Press (QPress) of the Center for Functional Nanomaterials (CFN), which is a US Department of Energy, Office of Science User Facility, at Brookhaven National Laboratory under contract no. DE-SC0012704. K.W. and T.T. acknowledge support from the JSPS KAKENHI (grant nos. 20H00354, 21H05233 and 23H02052) and World Premier International Research Center Initiative (WPI), MEXT, Japan, for hBN synthesis.

Author contributions

Y.Z. and L.G. conceived the project. L.G. fabricated the samples and performed the experiments. L.Z., R.N., S.P. and H.J. assisted with the sample fabrication. L.Z. and R.N. helped with the optical measurements. M.X., D.S.W., M.H. and Y.Z. contributed to the data analysis and

theoretical understanding. T.T. and K.W. provided the hBN samples. L.G. and Y.Z. wrote the paper with extensive input from the other authors.

Competing interests
The authors declare no competing interests.

Additional information
Supplementary information The online version contains supplementary material available at https://doi.org/10.1038/s41566-024-01434-x.

Correspondence and requests for materials should be addressed to You Zhou.

Peer review information *Nature Photonics* thanks Xi Wang and the other, anonymous, reviewer(s) for their contribution to the peer review of this work.

nature photonics

Article

https://doi.org/10.1038/s41566-024-01434-x

Giant optical nonlinearity of Fermi polarons in atomically thin semiconductors

In the format provided by the authors and unedited

Summary of Content

Section 1. Analysis of Anti-Crossing between IX_D and X_A

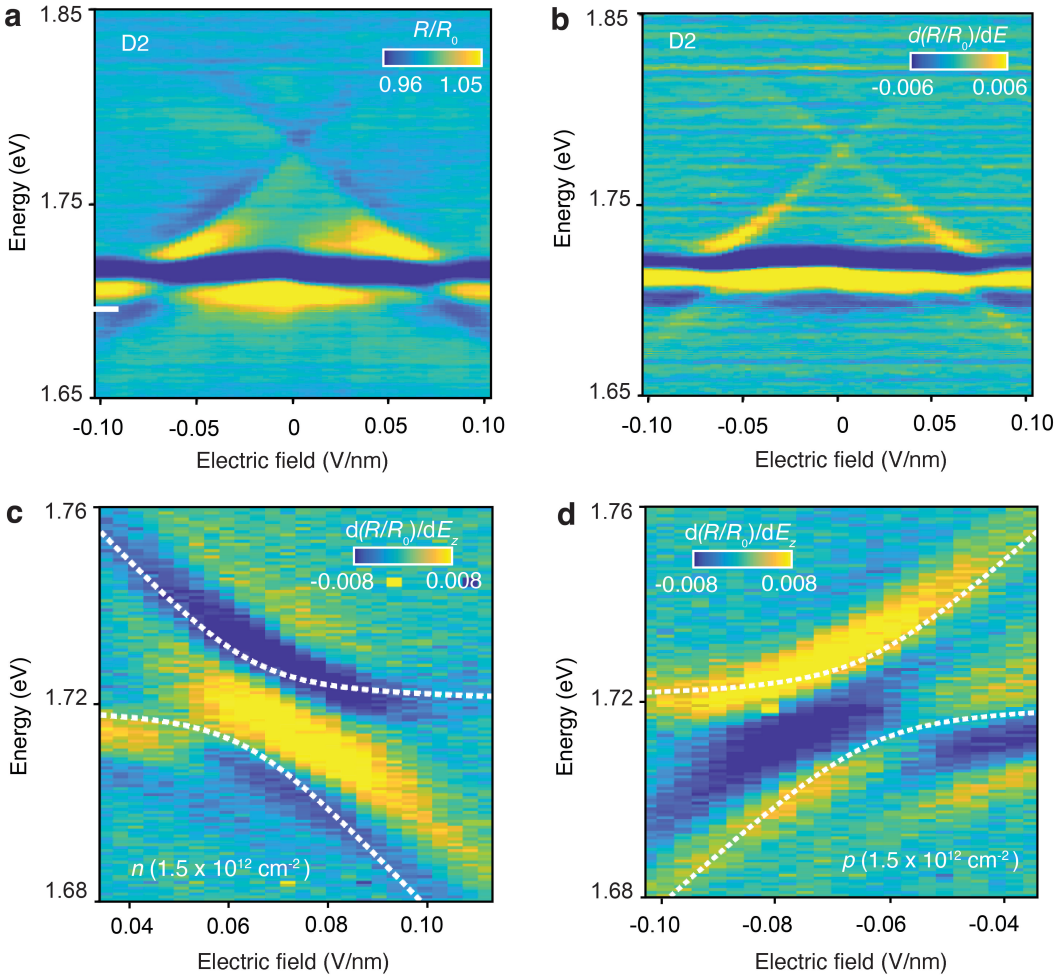

Figure S1 Anti-crossing between IX_D and X_A for various doping concentrations in device D2. **a,** Reflectance spectra (R/R_0) as a function of the electric field in the intrinsic regime. **b,** Differential reflectance spectrum (d(R/R_0)/dE) as a function of the electric field. The anti-crossing takes place at ~0.05 V/nm, consistent with device D1. **c, d,** Zoom-in view of the differential reflectance under electron (**c**) and hole(**d**) doped with an applied electric field. The white dashed lines represent the energies fitted with a two-level model. The fitted coupling strength **W** for electron and hole-doped side is around ~10 meV and comparable with that in intrinsic trilayer.

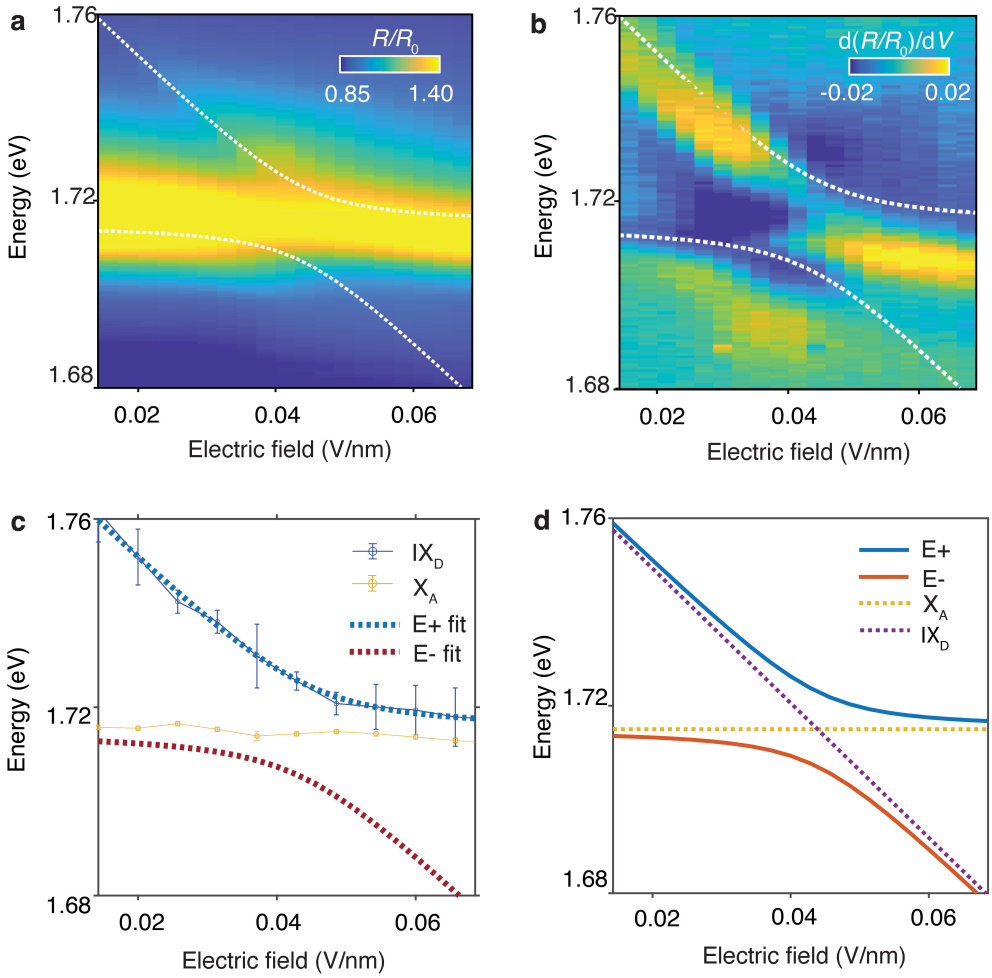

Figure S2 Analysis of anti-crossing between IX_D and X_A in device D1. a, Reflectance spectra (R/R_0) as a function of the electric field near the anti-crossing region. **b,** Voltage derivative of reflectance spectra, $d(R/R_0)/dV$. The white dashed lines in (a) and (b) represent the energies fitted with a two-level model. **c, d,** We study the anti-crossing between the IX_D and X_A based on a two-level system with a Hamiltonian:

$$H = \begin{pmatrix} E1 & W \\ W & E2 \end{pmatrix}$$

where E_1 and E_2 are the unperturbed energies of the IX_D and X_A, respectively, and W is the coupling strength. The new eigenvalues can be expressed as:

$$E_{\pm} = \frac{1}{2}(E_1 + E_2) \pm \frac{1}{2}\sqrt{(E_1 - E_2)^2 + 4|W|^2}$$

where $E_{\pm}$ correspond to the energies of the two branches. In (**c**), we extract the peak positions $E_{\pm}$ by fitting the reflectance spectra with the Lorentzian function. The error bars represent the variance of fitting peak energy. We then set E_2 to be 1.715eV, which is the mean energy of X_A, and keep it as a constant. E_1 is calculated based on the IX_D energy at zero electric fields and the stark shift. The stark shift slope k is estimated to be -1.436 eV/V in this particular device. The fitted anti-crossing is shown in (**d**) with a fitting parameter of $W = 10 \pm 2\ meV$.

Section 2. Doping-dependent photoluminescence map of trilayer WSe_2

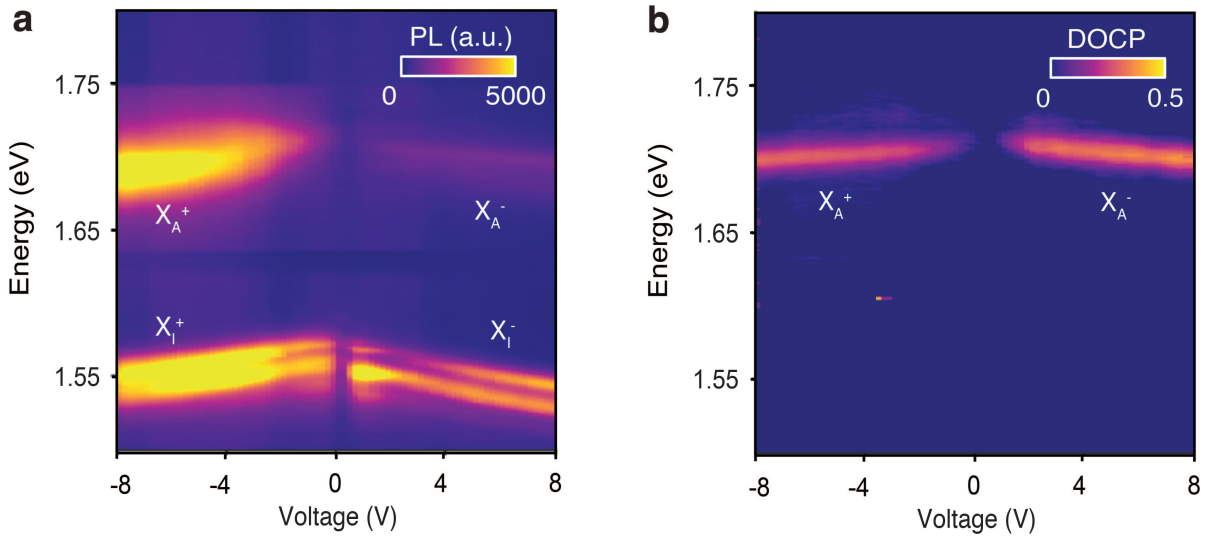

Figure S3 a, Doping-dependent photoluminescence of the trilayer WSe_2 at $E_z = 0$ taken from D2 at 4 K. b, Degree of circular polarization (DOCP) of the X_A^+ and X_A^-. The bright emission in the range of 1.5~ 1.6 eV corresponds to the momentum indirect trion/Fermi polaron. In contrast, the higher energy emission around 1.7eV corresponds to the momentum direct (K-K) intralayer trion/Fermi polaron. Both charged excitons X_I and X_A exhibit a redshift with increasing doping density.

Section 3. Effect of optical pumping on the oscillator strength of X_A^+

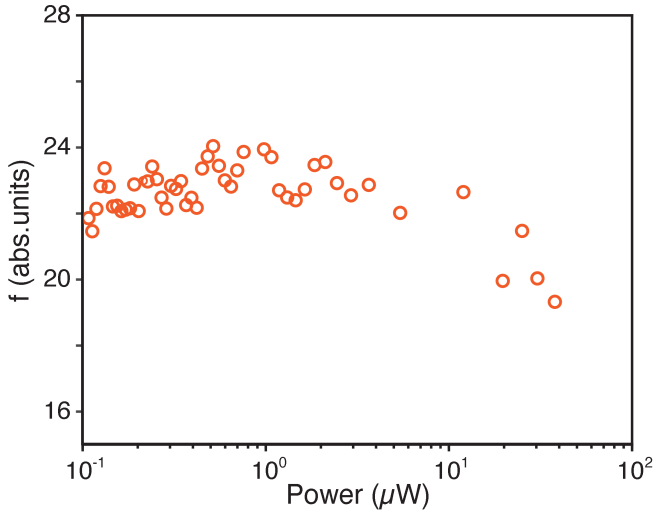

Figure S4 The oscillator strength of X_A^+, extracted from the reflectance spectra of sample **D3,** remains almost unchanged under low pump power and begins to decrease with increasing excitation power, when the blueshift becomes obvious.

Section 4. Optical nonlinearity under resonant excitation

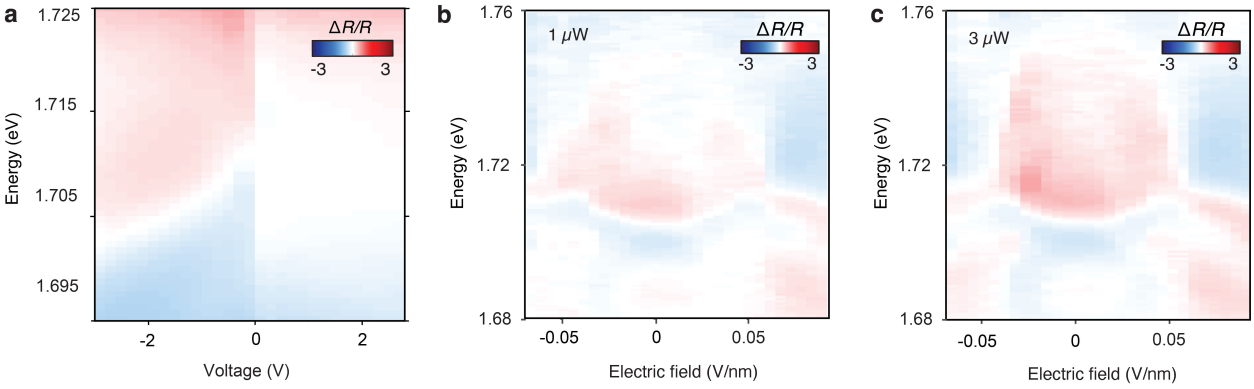

Figure S5. a, Relative change in the reflectance induced by 1 μW of resonant at resonant (718 to 730 nm) pulsed laser excitation under different doping. The color map is obtained by normalizing the reflectance change induced by the resonant excitation with respect to the reflectance without optical pumping, $\Delta R/R = \frac{R_{(1\,\mu W)}}{R_{(0.1\,\mu W)}} - 1$. The pulse has ~100 ps duration with a 40 MHz repetition rate. **b, c,** Reflectance change induced by a pulsed laser excitation power of 1 μW(**b**) and 3 μW(**c**), as a function of electric field, under hole doping. Under a small electric field, X_A^+ shows a blueshift, but it begins to redshift under excitation at a higher electric field. With increasing power, this transition point shifts to a lower electric field.

Section 5. Effect of pumping photon energy on nonlinearity

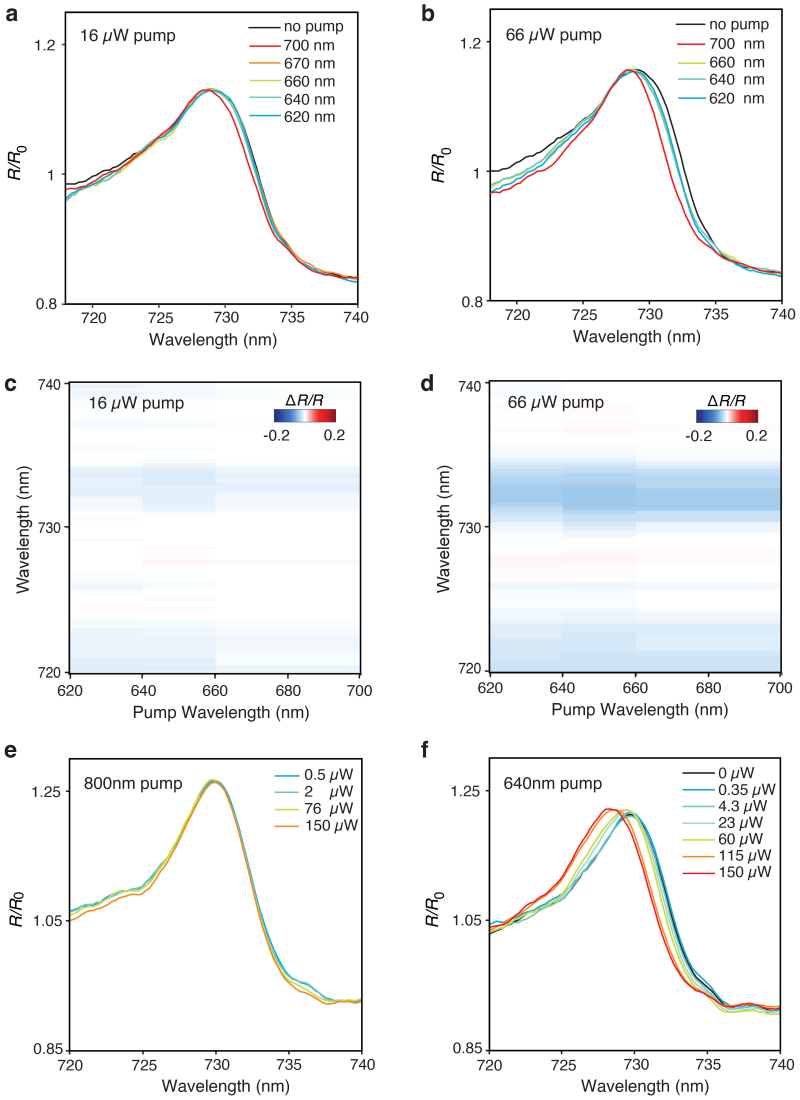

Figure S6 (a, b) Blueshift of X_A^+ under laser excitation at different center wavelengths (~10 nm spectral width) with a fixed pumping power at (a) 16 μW and (b) 66 μW. **(c, d)** The corresponding reflectance changes induced by optical pumping at different wavelengths show no significant wavelength dependence. **(e, f)** When exciting the system with photon energies below X_A^+, we did not observe significant blueshift (**e**), in contrast to higher energy excitation at 640nm (**f**). All data is acquired from device **D3**. We also note that the resonant excitation results in a much more pronounced blueshift (**Fig. S7**).

Section 6. Optical nonlinearity under different powers in various devices

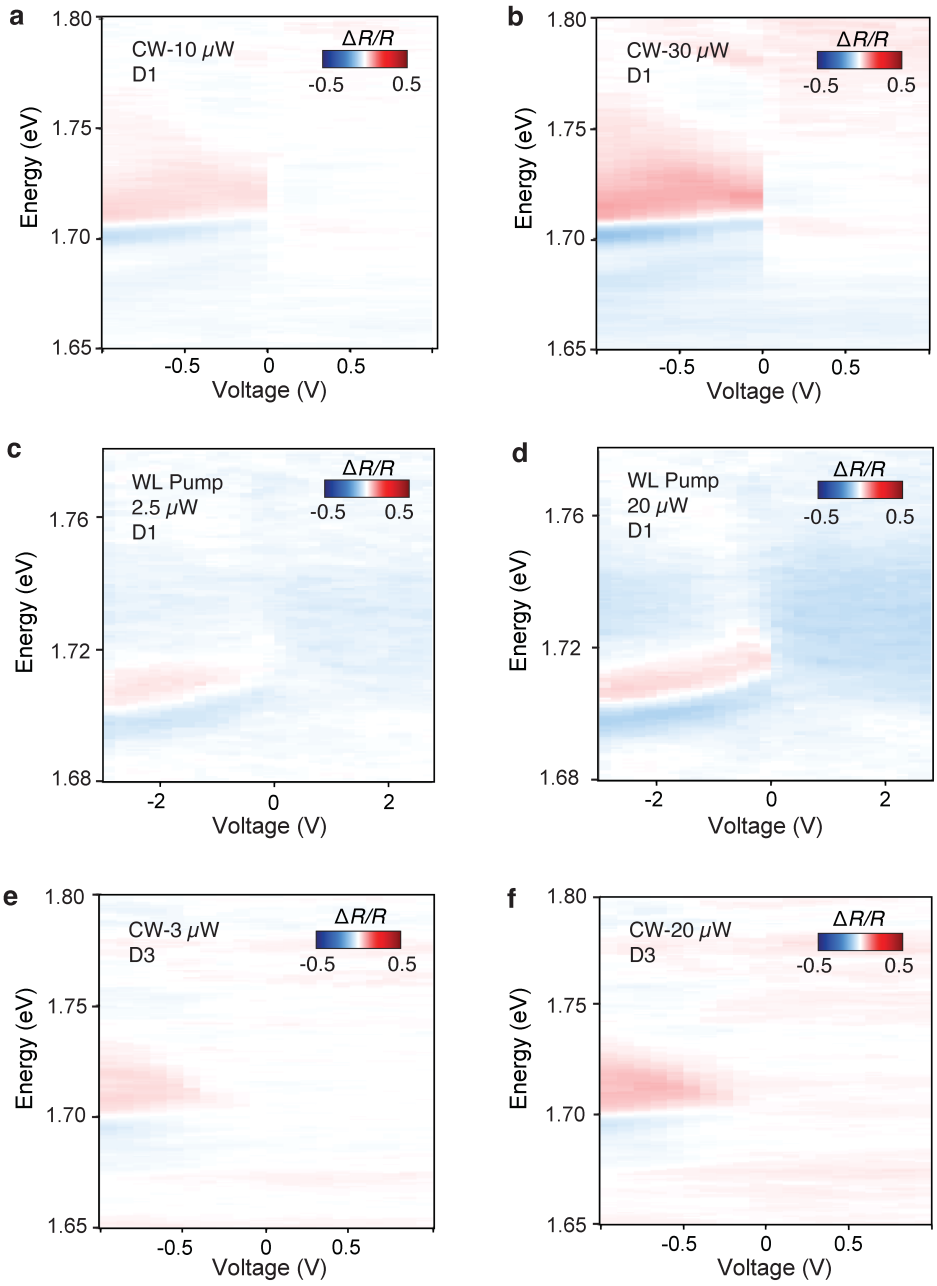

Figure S7 Relative change in the reflectance induced by optical pumping as a function of doping for various devices under different excitation conditions. We notice that the reflectance change is smooth near 0V, particularly at low excitation power. **(a)** 10 μW and high excitation power **(b)** 30 μW with 635 nm CW laser pumping for Device **D1. (c) 2.5** μW and **(d)** 20 μW 645nm pulsed laser excitation for device **D1. (e)** 10 μW and **(f)** 20 μW CW 635 nm laser pumping for Device **D3**.

Section 7. Effect of CW vs. pulsed excitation

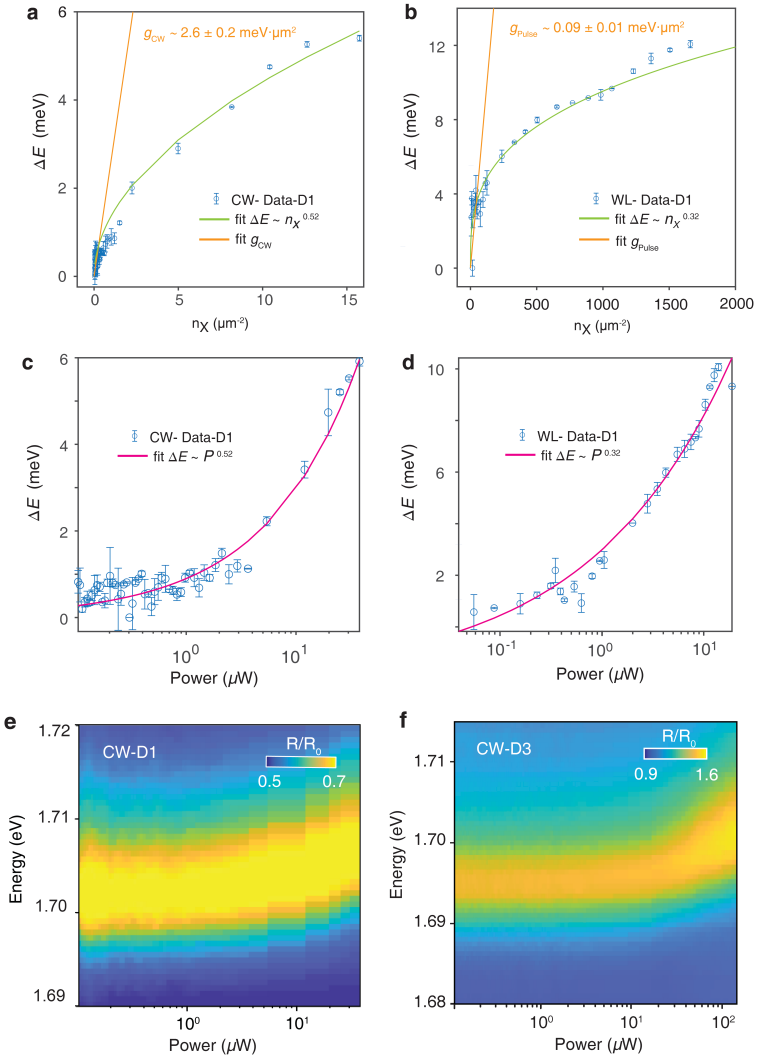

Figure S8 Analysis of power-dependent blueshift of X_A^+ under CW laser (a, c) and white laser excitation (b, d). a,b, Extraction of interaction strength g from (a) CW laser and (b) pulsed laser pumping induced X_A^+ blueshift vs. exciton density for **D1**. The exciton density is calculated from pump flux based on $n_X = P\alpha\tau/\hbar\omega$, where P is the pump power, α is the absorption coefficient, τ is the lifetime of the Fermi polaron, $\hbar\omega$ is the photon energy. The Fermi polaron lifetime is a few picoseconds, as measured in similar systems, and we use a value of 2 ps. The interaction strength is extracted from the linear fit of the $\Delta E - n_X$ curve in the low exciton density regime. The larger g values under CW excitation could be related to the complex relaxation dynamics of the exciton populations and an overestimation of exciton density under pulsed excitation. We also fit the blue shift amount as $\Delta E = a \cdot n_X{}^{(b)}$ over the entire data range. The fitting for CW laser and pulsed laser yields a coefficient of b as 0.52 with an R-square of 0.9516 for the CW laser and b of 0.32 with an R-square of 0.9317 for the pulsed laser, which shows a sublinear response for X_A^+ as polaron density. The hole doping density is kept at 8 x 10^{12} cm^{-2}. The error bars represent the variance of fitting peak energy. **c, d,** The same data as shown in **a, b**, plotted on a semilog scale,

to emphasize on the low power regime, with power as the x-axis. **e, f,** Power-dependent blueshift of X_A^+ under CW laser for **e,** device **D1** and **f,** device **D3**. The error bars represent the variance of fitting peak energy.

Section 8. Temperature dependence of X_A^+

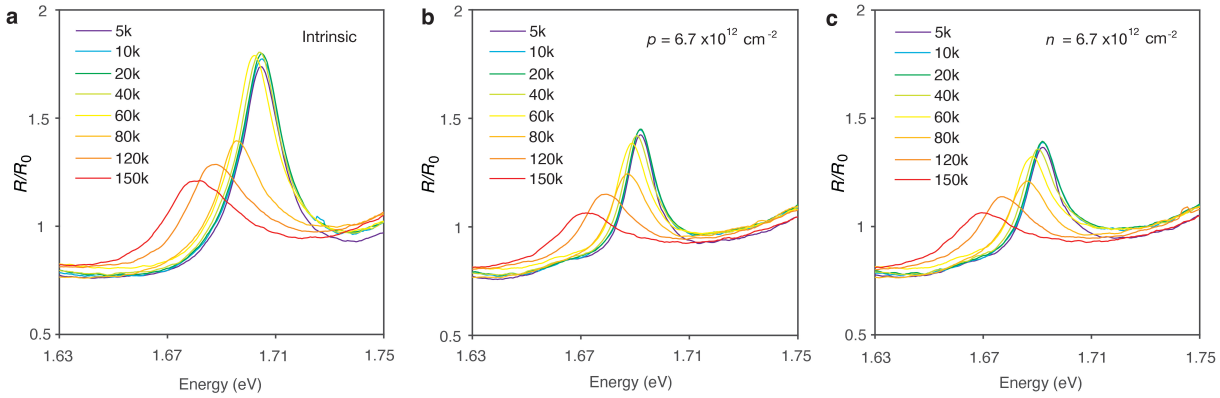

Figure S9 Temperature-dependent reflectance spectra of the trilayer under a constant doping density under zero electric field. In all cases, which include (**a**) intrinsic, (**b**) hole-doping, and (**c**) electron-doping, we observe strong redshift with increasing temperatures. Therefore, the observed nonlinearity, which corresponds to exciton blueshift, cannot be described as simple laser heating effects.

Section 9. Estimation of X_I density

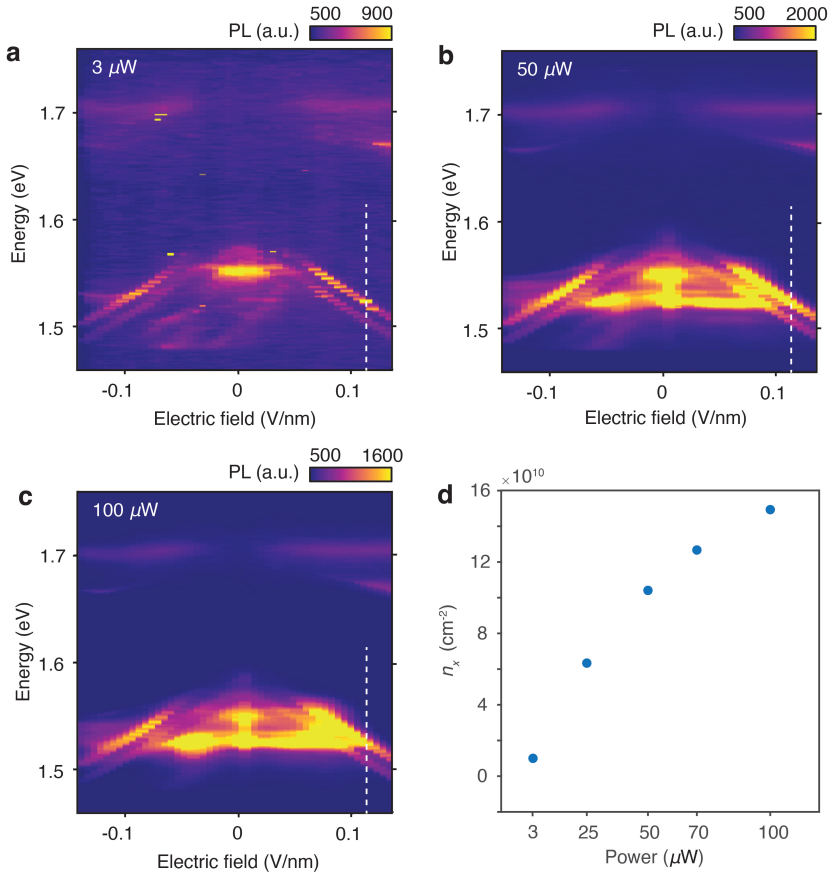

Figure S10 Estimation of X_I density as a function of pump power. a-c, Electric field-dependent PL map under different pump power (**a**) 3 μw, (**b**) 50 μw, (**c**)100 μw at the trilayer region. At an electric field of 0.12 V/nm, a maximum blue shift in a value of 3.3 meV of the X_I is observed. (**f**) X_I exciton density inferred from the above X_I blueshift under an applied electric field of 0.12 V/nm.

Section 10. Effect of circular polarization on Nonlinearity

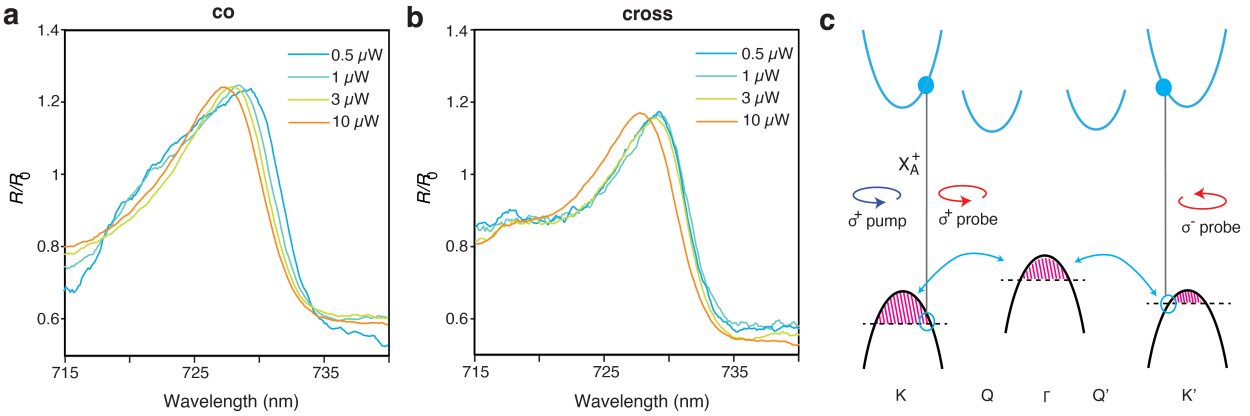

Figure S11 Valley-polarized holes under resonant circularly polarized excitation. (a, b) Power-dependent blueshift of X_A^+ under resonant pumping with **(a)** σ^+/σ^+ (pumping and probing K valley) and **(b)** σ^+/σ^- configuration (pumping K, while probing K' valley) when the sample is hole-doped. We observe a stronger blueshift of X_A^+ in **(a)**. We observe a stronger blueshift of XA+ in (a). In particular, we observe a ~1.3 nm blueshift under 3 μW pump when the pump and probe are co-polarized and no obvious shift in the cross-polarized case. Further increasing the pumping power to 10 μW leads to a blueshift in the cross-polarized setup, albeit still being smaller than the co-polarized case, which suggests the holes are partially polarized in K vs. K'. The data is acquired from device **D3**. **(c)** Nonequilibrium hole accumulation in K and K' valleys induced by selective valley pumping with a circularly polarized excitation. The resulting population imbalance between K and K' causes different amounts of blueshift in X_A^+ nonlinearity between the two valleys.

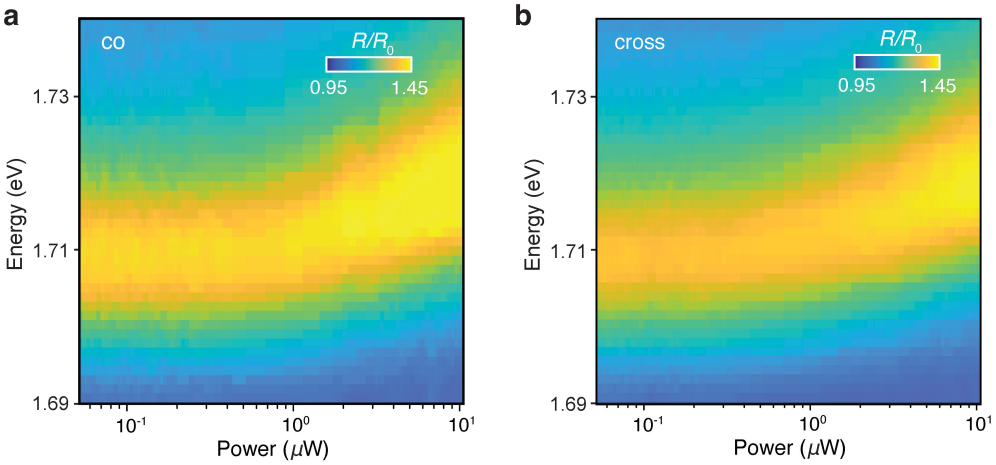

Figure S12 Non-resonant excitation with circular polarized polarization. Different from the resonant excitation case (**Fig. S12**), under non-resonant circularly polarized pump (635 nm), we observe similar magnitude of blueshift X_A^+ under **(a)** σ^+/σ^+ and **(b)** σ^+/σ^- configuration. This is

likely due to the breakdown of valley-selective optical selection rules far from the band edge as well as fast depolarization of excitons and electrons during the relaxation process.

Section 10. Electric-field tuning of Fermi polarons.

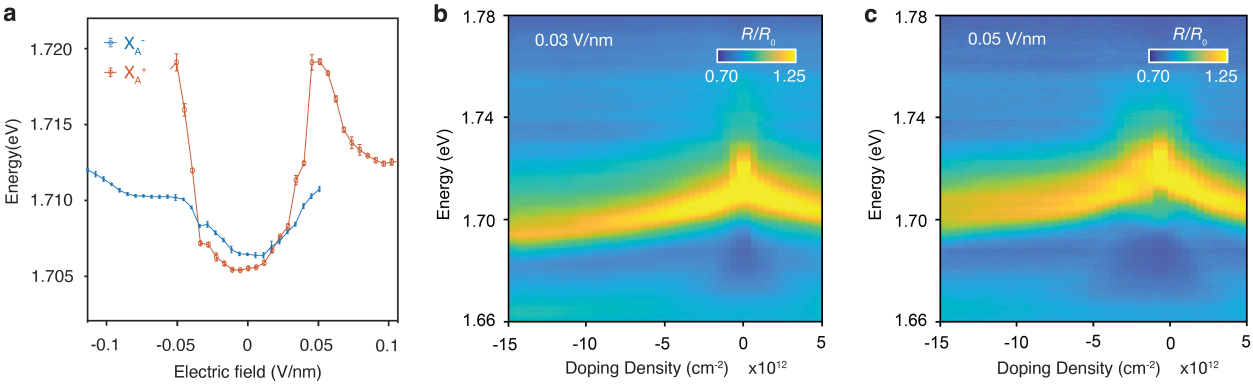

Figure S13 (a) Energy shift of X_A^- and X_A^+ with applied electric field with constant doping. The electron and hole doping densities are both kept at $4.9\times 10^{12} cm^{-2}$.The peak position is obtained by fitting the reflectance spectral with a Lorentzian model. The error bars represent the variance of fitting peak energy. **b,c,** Doping dependence of the intralayer Fermi polaron reflectance contrast R/R_0 in trilayer with applied (**a**) 0.03 V/nm, (**b**) 0.05 V/nm electric field. The negative doping density represents hole hole-doped side. An obvious blueshift and broadening of X_A^+ is observed on the hole side with an increasing electric field, corresponding to the additional phase space filling due to the population transfer from Γ to K valleys. Such a shift is much weaker on the electron side.

Section 11. Comparison of nonlinearity with previous work

Table S1

Here, we compare the amount of blueshift per pump power, which has important implications for low-power devices. Indeed, in our current work, much smaller pump power is needed to shift the absorption of excitons by a similar amount, in comparison with previous reports. This is related to the fact that the measured interaction strength g is much larger than previous reports and theoretical exchange/dipolar interactions. We also note that while one can observe a significant shift of interlayer excitons at relatively low power (Ref. [4, 5]), these species have negligible absorption because of long lifetime, as we discussed in the introduction of the paper.

	This work*	Ref. [1]	Ref. [2]	Ref. [3]	Ref. [4]	Ref. [5]
Species	Fermi Polaron	Hybridized Interlayer Exciton	Interlayer Exciton	2*s* Exciton Polariton	Interlayer Exciton	Interlayer Exciton
n_x (cm^{-2})	10^9	~$4*10^{12}$	~$2*10^{10}$	~$6*10^9$	$1.2*10^{11}$	~10^{12}
ΔE (meV)	6	~7	~2.2	1-2	~2	~22
Power ($\mu W/\mu m^2$)	37	$3.25*10^6$	1300	$3*10^4$	60	~300
System	Trilayer WSe_2	Bilayer MoS_2	Bilayer MoS_2	Monolayer WSe_2	Bilayer WSe_2	$MoSe_2$/ hBN/ WSe_2
Probe	Absorption	Absorption	Absorption	Absorption	PL	PL

References:

1. Datta, B. *et al.* Highly nonlinear dipolar exciton-polaritons in bilayer MoS2. *Nat. Commun.* **13**, 1–7 (2022).
2. Louca, C. *et al.* Interspecies exciton interactions lead to enhanced nonlinearity of dipolar excitons and polaritons in MoS2 homobilayers. *Nat. Commun.* **14**, 3818 (2023).
3. Gu, J. *et al.* Enhanced nonlinear interaction of polaritons via excitonic Rydberg states in monolayer WSe2. *Nat. Commun.* **12**, 2269 (2021).
4. Wang, Z., Chiu, Y.-H., Honz, K., Mak, K. F. & Shan, J. Electrical Tuning of Interlayer Exciton Gases in WSe_2 Bilayers. *Nano Lett.* **18**, 137–143 (2018).
5. Sun, Z. *et al.* Excitonic transport driven by repulsive dipolar interaction in a van der Waals heterostructure. *Nat. Photonics* **16**, 79–85 (2022).